Preliminary Characterisation of Titanium Nitride Thin Film at 300 mK for the Development of Kinetic Inductance Travelling Wave Parametric Amplifiers

Joseph Longden[a*], Faouzi Boussaha[b], Christine Chaumont[b], Kitti Ratter[a†], and Boon-Kok Tan[a]

[a]Dept. of Physics (Astrophysics), Univ. of Oxford, DWB Keble Road, OX1 3RH, Oxford, U.K.
[b]GEPI (CNRS UMR 8111), Observatoire de Paris, PSL Université, France.

ABSTRACT

Travelling wave parametric amplifiers (TWPAs) made from highly nonlinear reactive superconducting thin films have been demonstrated to be a viable technology for various quantum applications, including fundamental physics experiments such as astronomy and axion dark matter searches, as well as commercial applications like quantum computational and communication systems. In this paper, we present the design of a kinetic inductance TWPA comprising a patterned titanium nitride film that can operate at 0.3 K to demonstrate the feasibility of operation closer to 1 K temperature, paving the way to achieve even higher bath temperature operation. We discuss in detail the design of our TWPA, along with the predicted gain-bandwidth product and other characteristics. We perform the preliminary experimental investigation of the thin film properties and compare that with the simulated results. We found that there are several discrepancies between the measured and the predicted behaviour of the thin film. We attribute these differences to the fact that the fabricated thin film has a different gap voltage, resistivity and thickness to what we expected. With a new set of estimated parameters, we successfully reproduce the measured transmission profile. We further show that by utilising bridges to ensure equipotential grounds for the CPW lines, we managed to reduce the rippling effect and achieve higher gain with broader bandwidth. We expect that our TWPA can achieve higher than 20 dB gain from approximately 0–8 GHz.

Keywords: Low-Noise Amplifier, Superconducting Thin Film, RF Microwave, Travelling-wave, Kinetic Inductance, Quantum-Limited

1. INTRODUCTION

Broadband amplifiers with quantum-limited noise performance are important for many applications, especially ultra-sensitive cryogenic detection systems such as astronomical receivers,[1–5] dark matter search experiments[6–8] and quantum computation.[9–13] Traditional low noise amplifiers (LNAs) such as high electron mobility transistor (HEMT) amplifiers or Josephson parametric amplifiers (JPAs) either struggle to reach the quantum noise limit or only have a very limited operational bandwidth. There has, therefore, been interest in developing a broadband amplifier technology capable of achieve quantum-limited noise performances. The invention of microwave superconducting travelling wave parametric amplifiers (TWPAs) in the past decade[14–16] have since opened up a new avenue for achieving such high gain over GHz bandwidth, instead of MHz, with quantum limited noise performance. Their negligible heat dissipation and ease of fabrication also makes them readily scalable to arrays for large pixel count applications.

TWPAs achieve high gain via wave mixing mechanisms, where the energy from a strong pump tone is transferred to a weak detected signal along a long, low-loss, non-linear transmission line. The non-linearity is typically achieved either by utilising the kinetic inductance of a superconducting wire (namely kinetic inductance (KI-)TWPA) or a series of Josephson junctions (in some cases superconducting quantum interference devices (SQUIDs)) embedded along a transmission line. In this paper, we focus on the development of KITWPA.

*E-mail: joseph.longden@physics.ox.ac.uk
†Now at National Physical Laboratory, Teddington, UK

Most of the KITWPA reported in the literature operate at $\ll$100 mK environment, making them unfavourable for high temperature applications. In this paper, we present a KITWPA comprising a patterned titanium nitride (TiN) film with a critical temperature (T_c) of 4.39 K such that the TWPA can be operated at a higher bath temperature. We hope to demonstrate the feasibility of operation at higher temperatures, paving the way for TWPA operation at liquid helium temperature, thereby removing the barrier-of-entry for many applications that are not operating at mK regime. Our TiN wire is periodically altered to provide means for dispersion control and suppression of higher harmonics. The prior is to promote exponential instead of quadratic gain, while the latter ensures efficient energy transfer to the incoming signal. We shall discuss in detail the design of our TWPA, presenting the predicted gain-bandwidth characteristic and compare that with the preliminary experimental results of the device measured at 0.3 K in the following sections.

2. DESIGN & SIMULATION

Fig. 1 (a) and (b) illustrate the design of our periodically loaded KITWPA centred at ~8 GHz. The 100 nm thick TiN film with a normal resistivity $\rho = 140\ \mu\Omega$cm is deposited on a 500 μm thick high resistivity silicon substrate. The main transmission line is formed using a coplanar waveguide (CPW) with the central strip and gap width optimised to achieve characteristic impedance $Z_0 = 50\,\Omega$. At the loading sections, these dimensions are altered, resulting in $Z_0 \neq 50\ \Omega$ at $\sim \lambda_c/6$. At every third loading section, the CPW dimension is altered again to produce the 'child' stopbands. These stopbands are illustrated in Fig. 1 (c), where the primary loading sections create

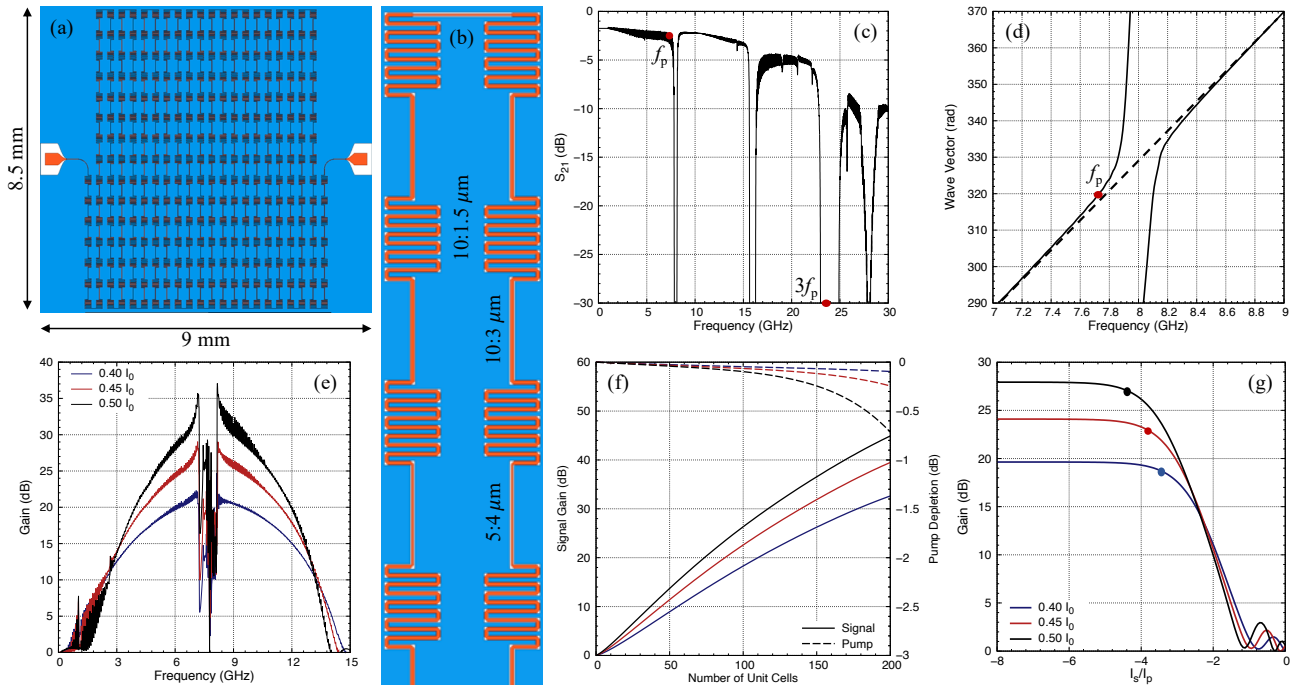

Figure 1. (a) Layout of our KITPWA with 105 cascaded unit cells and the bonding pads. A unit cells is formed from a set of three 50 Ω sections and three loading sections with the third of these loading sections having a different CPW dimension. (b) Zoom in on a section of the CPW transmission line, showing the 50 Ω sections and the loading sections with their respective central strip and gap widths. (c) The predicted transmission profile of the entire chip, clearly showing the stopbands caused by the periodic loadings. (d) The divergence of the dispersion relation around the first stopband near 8 GHz where the pump is located. (e) The predicted gain profile of the TWPA with pump frequency at 7.706 GHz with various amplitudes of the pump current. The same colour scheme is used for the remaining of the plots. (f) Peak gain at 6 GHz in relation to the total length of the TWPA. Note that the position of the peak gain is not fixed for a certain transmission length as it is dependent on the pump power, hence there is no optimal length of the TWPA. (g) The –1 dB compression point of the TWPA at 6 GHz in relation to different pump current. Note that the x-axis is the power index of 10, hence a log scale.

the large attenuation gap near 24 GHz. The subsequent 'child' gaps near 16 and 8 GHz are caused by the third loading sections. As the pump is expected to be located around 8 GHz, we see that the third harmonic of the pump tone (the KITWPA is a Kerr χ_3 line) will fall within the primary stopband gap, severely suppressing its formation (and hence other higher harmonics as well as shock wave formation).

It is well known that to achieve high gain, the power dependent phase difference between the pump, the detected signal and the generated idler needs to be minimised. This can be done by correcting the phase mismatch between all waves with an additional phase added to the pump waves, via a technique called dispersion engineering. As shown in Fig. 1 (d), these stopbands not only provide a large attenuation band for harmonic suppression, but also cause the dispersion (or wave vector) to diverge rapidly away from an otherwise linear relation. By placing the pump near these divergences, we can alter the total phase of all waves travelling along the transmission line to achieve near-perfect phase matching. Three of these loading sections along with three sets of 50 Ω CPW lines form a single unit cell, which is cascaded 105 times to form the entire chip. The length of such unit cell corresponds to half the wavelength of the central frequency. We meandered the long CPW line to produce a compact design.

The pump-power dependent gain-bandwidth product of our KITWPA is calculated using the standard coupled mode equations including the losses of the transmission line[17] and is shown in Fig. 1 (e). Unsurprisingly, the maximum gain increases with higher pump power, although it is unfavourable to use a higher pump current than required, as the coupled mode equations operate under the assumption that $I_p \ll I_0$ (where I_p and I_0 are the amplitude of the pump current and the critical current value of the film respectively) and higher pump current could potentially induce higher losses in terms of resistive heating. As shown in the figure, we expect to achieve close to 20 dB gain between approximately 4.5 GHz and 11.5 GHz with $I_p = 0.45\ I_0$.

Fig. 1 (f) shows the relation of the signal gain with the total length of the TWPA i.e., the number of unit cells. Due to the intrinsic losses of the transmission line e.g., residual surface resistance, dielectric/substrate losses etc, the parametric gain will not increase infinitely along the length of the transmission line but peak at a certain length. The location/length of this peak is influenced by two factors. The first is where the magnitude of the losses becomes higher than the gain, resulting in the signal gain beginning to be depressed. The second is at high gains, where the amplitude of the signal wave is closer to or even higher than the pump, the energy starts to transfer back to the pump, and the signal amplitude is depleted. Note that the optimal length or the location of the peak gain in dependent on the magnitude of the pump current and in our case, we have not yet reached the optimal peak gain, which we expect to be beyond 200 unit cells with I_p in the range of 0.4–0.5 I_0.

Finally, we estimate the compression point of our TWPA, as shown in Fig. 1 (g). Again, the –1 dB compression point moves with the pump power. The compression plot shows that it is preferable to operate the TWPA with a lower pump current as a higher I_p reduces the compression point e.g., by an order of magnitude if I_p increases from 0.4 to 0.5 I_0. At $I_p = 0.45\, I_0$, we see that the signal gain will drop by 1 dB when the detected signal amplitude is about $10^{-4}\, I_p$. Taken that $I_0 \approx 3$ mA, this translates to a pump power of –10.4 dBm and a signal power of –90.4 dBm.

3. EXPERIMENTAL SETUP

Our TWPAs were fabricated at the Observatoire de Paris using their clean room facilities and delivered to the University of Oxford for characterisation in a cryogenic environment. The testing of the TWPA samples was carried out in a 300 mK refrigerator designed and built at the University of Oxford with a cryo-cooler provided by Chase Research Cryogenic ®. Fig. 2 (a) shows a schematic of the experimental setup within the cryostat. A signal tone is generated by a vector network analyser (VNA) at room temperature and its amplitude is reduced by a series of warm and cold attenuators before being fed into the TWPA mounted at the 300 mK cold plate. The output from the TWPA is connected to a superconducting coaxial cable and subsequently to a commercial cryogenic low-noise amplifier (LNA) located at the 4 K plate, which is used to boost the amplified signal above the room temperature noise floor. After further warm amplifications, the amplified signal is routed back into the VNA for analysis. In some cases, the VNA is replaced with a synthesiser and a spectrum analyser for simple single tone measurements. The pump tone is generated either by the VNA or the synthesiser, before passing through a splitter where half of the output is attenuated to 300 mK stage before being coupled into the TWPA,

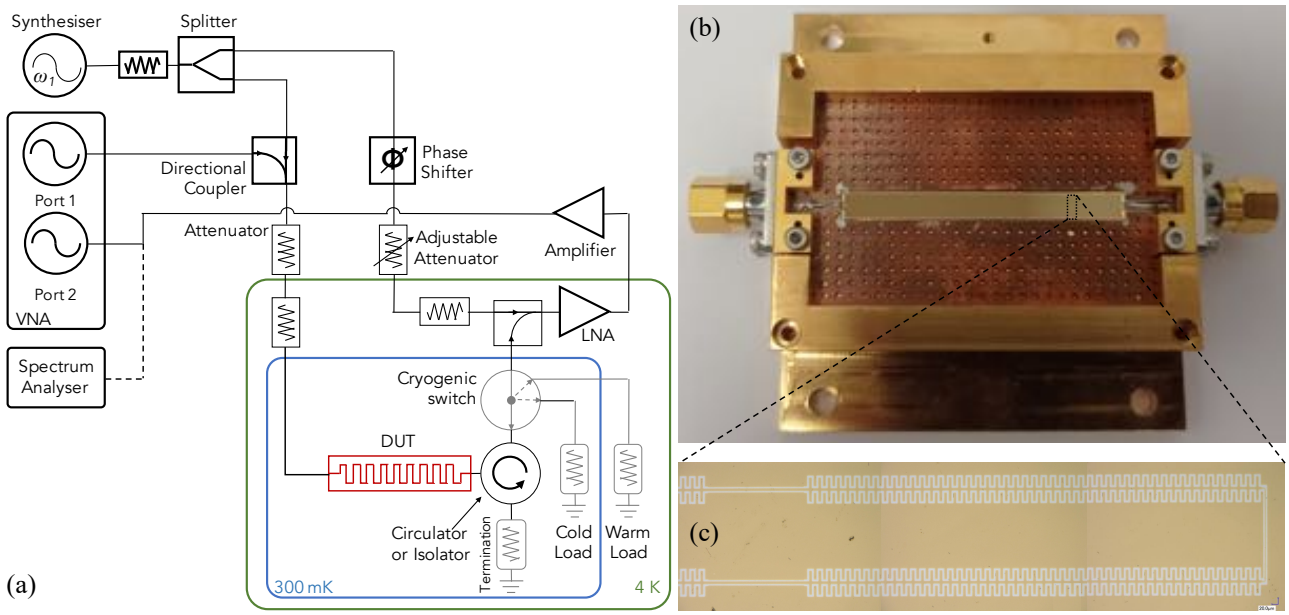

Figure 2. (a) Diagram of the experimental setup. Components for noise measurement were not installed in the system at the moment of writing, hence are greyed out in the diagram. (b) Image of the TWPA chip installed in a sample holder. The chip dimension is 4.2 mm×44 mm. The sample holder is larger than needed to accommodate various other samples of different sizes. The covering lid is not shown in the figure. (c) Microscope image of a portion of the printed transmission line.

and the other half is attenuated and phase shifted to cancel out the residual pump tone from the output of TWPA to prevent saturation of the LNA.

Fig. 2 (b) shows an image of the fabricated TWPA sample mounted in a gold-plated copper sample holder, with the zoomed-in microscope photo of the patterned TiN transmission line in 2 (c). The TWPA sample is wire bonded to a copper-clad grounded coplanar waveguide etched into a 0.51 mm thick Rogers Duroid® RO4350b printed circuit board (PCB) connected to the required SMA interfaces. We use both gold and aluminium bond wires of 80 μm diameter to thermalise the chip (via the gold bond wires) as well as providing good electrical connection with superconducting aluminium. The sample chip sits directly on top of the bottom plate of the sample holder, within the cutout slot of the copper PCB to provide better thermalisation of the chip to the base plate. The chip is held within the sample holder cutout with silver electrodag around the corners before wire bonding. The two grounding patches of the CPW lines fabricated on top of the PCB is connected to the bottom ground plane through a grid of plated via holes. The PCB itself is clamped down with two side bars which provide the mean for attaching the covering lid as well (lid not shown in the image). The sample holder is designed such that it can be used with or without the lid, and the copper PCB can be replaced with different cutout sizes to accomodate various sized TWPA chips.

4. TRANSMISSION PROFILE AND THIN FILM CHARACTERISTICS

Before we proceed to measure the gain-bandwidth product and the noise performance of our TWPA, we first characterise the transmission profile and the thin film properties in order to ensure that the film is fabricated to the specification listed above. Fig. 3 (a) shows the transmission S_{21} spectrum of the TWPA with an input power of –60 dBm at a bath temperature of 360 mK. Comparing this to the simulated spectrum shown in Fig. 1 (c), we noted a number of discrepancies between the two. First, the spectrum is very noisy with regular ripples oscillating up to 10 dB from the smoothed fit. Second, the measured transmission spectrum is significantly lower than the simulated equivalent, suggesting that the TWPA chip is much lossier than we expected. Third, the

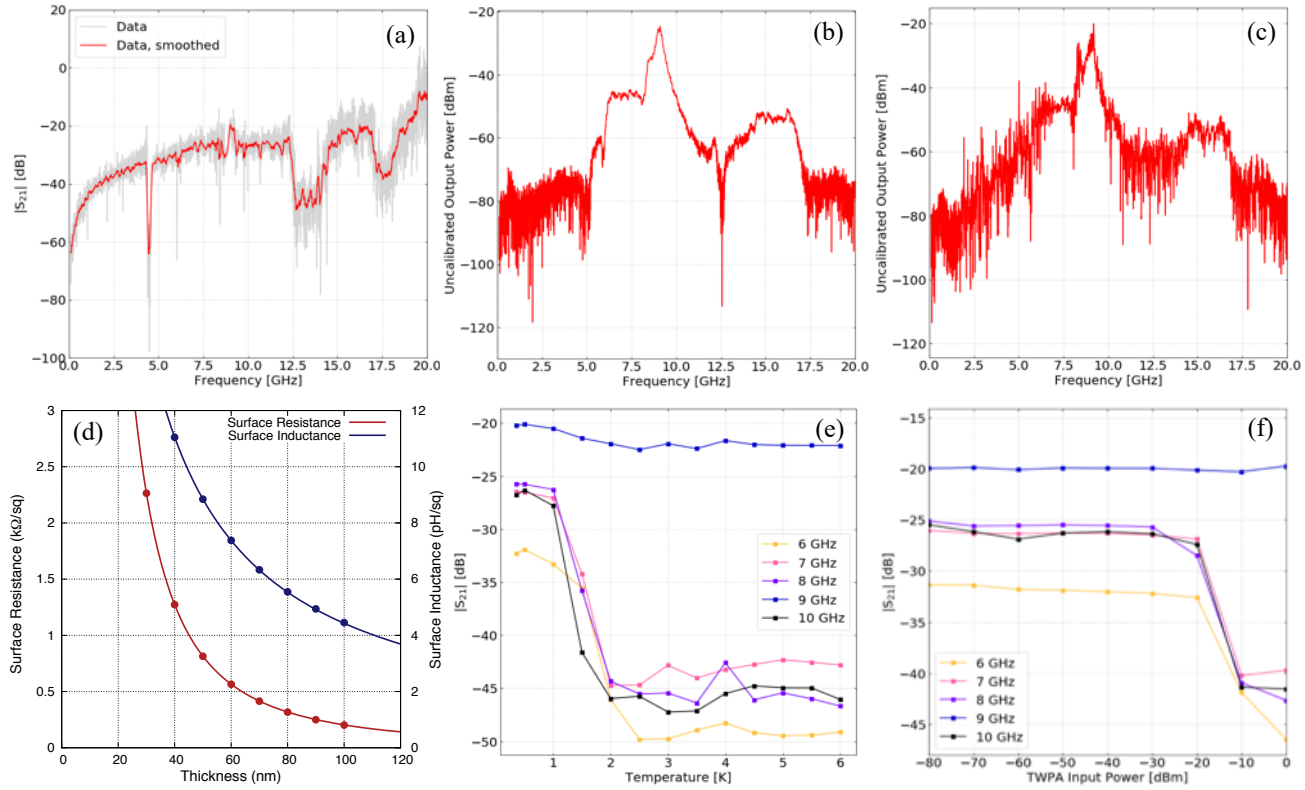

Figure 3. (a) Measured TWPA transmission spectrum at 360 mK with an input power of –60 dBm. (b) Uncalibrated S_{21} spectrum through the TWPA chip at room temperature in the absence of radiation shields and (c) in the presence of radiation shields. (d) Calculated surface resistance and inductance values with relation to the TiN film thickness. (d) Measured transmission as a function of bath temperature for an input power of –60 dBm from the VNA. (f) Measured transmission as a function of input power at a bath temperature of 360 mK.

dispersion features i.e., the stopbands are shifted to different frequencies compared to simulation, and finally, it appears that there is an unexplained low frequency cutoff below 2.5 GHz.

There are several potential root causes for these unexpected transmission behaviours. The presence of the ripples could be attributed to the radiative nature of our CPW transmission line which was fabricated without any air bridges to ensure an equipotential ground on both side of the CPW. As pointed out by Shu et. al.,[18] the discontinuities could excite slotline modes which are radiative, in particular the 90° bends that exist throughout the entire chip. As shown in Fig. 3 (b) & (c), we observed that even at room temperature the ripples disappear and the transmission profile is much cleaner when we surrounded the sample with Eccosorb ® absorbers. These unwanted radiative modes could also explain why the TWPA chip is much lossier than we expected. Furthermore, we suspect that the long transmission line could be capacitively opened or inductively short, which most probably is the latter as the CPW gap is much smaller than the central strip width and the chip is fully exposed without any protective layer on top of the TiN film. This could explain why we see higher than expected transmission loss in addition to the radiative losses, especially at low frequencies. The existence of the inductive short could also induce an unexpected resonance in the chip, in conjunction with the existing geometric capacitance along the transmission line. This potential resonance is hinted in Fig. 3 (b) & (c) where we see a transmission peak near 9.5 GHz and a subsequent dip at 12.5 GHz. This transmission peak is not caused by the box resonance, as its existence is unaltered by the removal of the sample holder's lid. We also observed that the magnitude and location of this peak is independent of the base temperature, further indicating that there is some unexpected low-Q resonance caused by the inductive shorts along the transmission line.

As shown in Fig. 1 (d), we expect that the lowest stopband would be located near 8 GHz, with subsequent

S_{21} dips at the vicinity of 16 GHz, 24 GHz etc. We clearly observe however, that the lowest stopband measured in Fig. 3 (a) is shifted to 4.5 GHz and the primary stopband at 24 GHz is now lowered to around 13.5 GHz (the missing second dip around 9 GHz is masked by the unexpected resonance feature around this frequency, as explained earlier). This suggests that the electrical length of our transmission line is now close to double the value we expected. This further indicates that the surface impedance of the thin film is higher than the designated value. If this is the case, not only will the change in surface impedance alter the transmission length, it also impacts the characteristic impedance of the transmission line, causing it to deviate from the intended 50 Ω value. This could contribute the existence of the large ripples in the transmission curve, as there is now a large impedance mismatch between the chip and the external circuitry.

There are several reasons why the surface impedance is higher than we expected. It could be that the thin film resistivity is higher than the intended 140 $\mu\Omega$cm value, the gap voltage hence the critical temperature of the film is lower, or the film is thinner than we expected (see Fig. 3 (d)). The actual resistivity and the thickness of the film is difficult to measure on-chip without having another sample made during the fabrication of these devices, as the fabrication condition could be different with different batches. Instead, we can measure the transmission spectra at various bath temperatures to ascertain the critical temperature (T_c) of the superconducting film, and hence the actual gap voltage. Fig. 3 (e) shows the S_{21} spectrum as a function of temperature for an input power of –60 dBm. At lower temperatures, the transmission is relatively high, suggesting the film is in its superconducting state. Beyond 1 K, we observe that the transmission drops by close to 2 orders of magnitude, indicating that the film is approaching its normal state. The exception to this trend is the 9 GHz plot, which again is the frequency where we suspect the temperature-independent unexpected resonance lies. Whilst our TiN films have a predicted T_c=4.39 K, our measurement results are contradictory to this, as the level of transmission begins to decrease just above 1 K. It is worthwhile noted that the data shown were obtained when the cryostat is in the process of cooling down, which may leave inadequate time for the sample to thermalise properly with the base plate. We suspect, however, that the actual T_c is still much lower than the expected value of 4.39 K.

Finally, we measured the critical current I_c of the film to gain a better insight into the properties of the TiN film. Fig. 3 (f) shows the S_{21} transmission as a function of input power at a bath temperature of 360 mK. In the superconducting state, it is expected that the transmission stays constant with increasing input power until it exceeds the critical current value, where the film transitions to the normal state and the transmission decreases. The experimental data shows the transmission remains relatively flat across the input power range until about –20 dBm. A maximum input power of –20 dBm corresponds to a critical current of about 0.5 mA, which is about the correct order of magnitude for our TiN film.

5. RE-SIMULATING THE TWPA BEHAVIOUR

With the measured parameters obtained above, we re-simulated our TWPA model to predict the expected performance of the TWPA. We assume that the critical temperature is close to 1.5 K, corresponding to a V_{gap} of 0.45 mV. From previous experiments, we have learnt that the resistivity of the TiN film increased to about 175 $\mu\Omega$cm for a film with V_{gap} =0.45 mV, and as we suspect the film might be thinner than intended, we have run our new simulation with slightly thinner film, 75 nm instead of 100 nm.

As shown in Fig. 4 (a), we can clearly see that with the new set of parameters, the stopband positions are now closer to the frequencies we measured earlier e.g., the first stopband is now approaching 4.5 GHz. The new simulation also predicts much lossier transmission and slightly stronger rippling effect, in agreement with our measurement results presented earlier. Note that the loss is also much severe at higher frequency end, and we believe the higher loss shown here is caused by the transmission line is now having a characteristic impedance of $Z_0 \neq$50 Ω, hence a strong impedance mismatch between the TWPA and the 50 Ω environment.

By placing our pump at 4.602 GHz, it appears that we should still be able to achieve higher than 20 dB gain from about 2.5–6.5 GHz, with a pump current of 0.45 I_0. Fig. 4 (b) shows the gain profile of the TWPA with pump current from 0.4–0.5 I_0 as before. The gain at the upper half of the gain profile is slightly lower than the lower half, caused by the higher loss between 5–10 GHz compared to below 5 GHz. This is also in contrast with previous simulated S_{21} profile which shows similar transmission magnitude above and below 5 GHz. Although the zero-gain gap near the middle of the gain profile seems larger than the original design, it is in fact the same

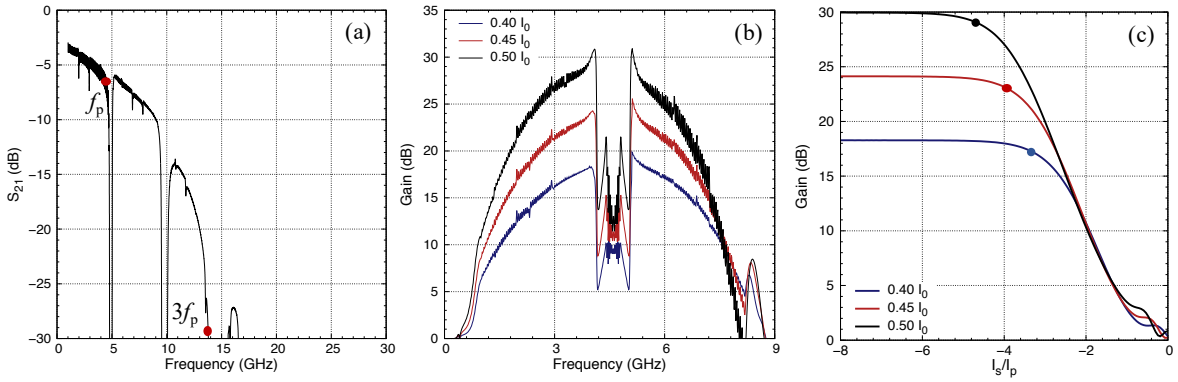

Figure 4. (a) The re-simulated transmission profile of the TWPA chip with new parameters, with the stopbands closer to the measured frequencies. (b) The predicted gain profiles of the TWPA with pump frequency at 4.602 GHz. (c) Re-simulated –1 dB compression point of the TWPA at 4 GHz in relation with different pump current.

bandwidth around 1 GHz wide. Similarly, we plot the new –1 dB compression point in Fig. 4 (c) and it indicates that we can still obtain the same compression point of $I_s = 10^{-4} I_p$ for the case of $I_p = 0.45\, I_0$.

Finally we investigate the effect of employing multiple bridges across the CPW line to ensure the two lateral ground planes of the CPW are always equipotential along the long transmission line, and therefore suppress the unwanted modes which we suspected are radiative and inducing high loss. In our model, the bridges are formed using a 100 nm thick TiN film fabricated on top of a 200 nm silicon monoxide (SiO) dielectric layer, which stacked above the original TiN film. The SiO layer covers the entire area of the TWPA chip, except the edges and the bonding pads for ease of wire bonding. This dielectric layer therefore also act as a protective film for the patterned bottom TiN line to prevent any unintentional inductive short during handling of the TWPA chips. Fig. 5 (a) shows the positions of these bridges along the TWPA transmission line, where they are placed primarily near the two ends of the loading sections.

As can be seen clearly from Fig. 5 (b), with these added bridges, the transmission profile is now much cleaner compared to the one shown in Fig. 4 (a). The transmission ripple is minimised and the S_{21} behaviour is also much more uniform and predictable with less loss at the higher frequencies. Note that the stopband frequencies now shifted slightly lower, as the added bridges increase the shunt capacitance hence effectively increase the electrical wavelength of the transmission line, although the effect is marginal.

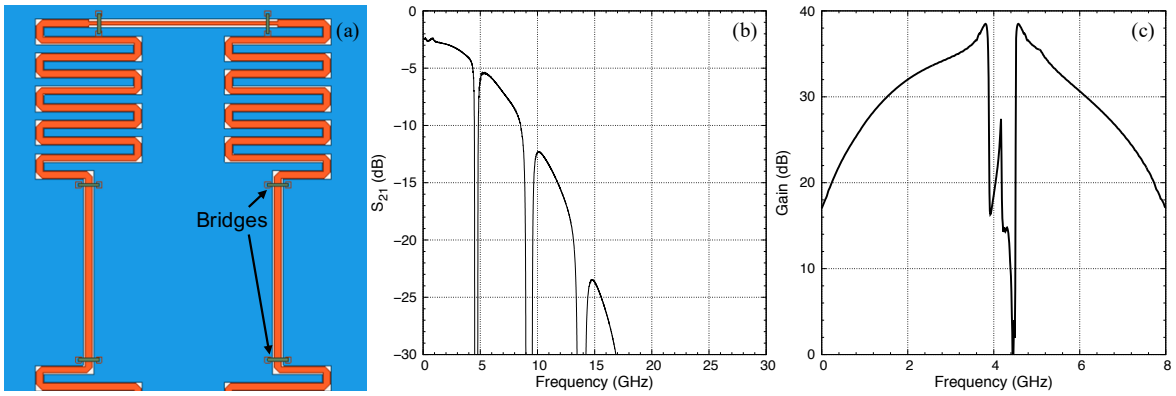

Figure 5. (a) Bridges were added at the beginning and the end of each loading sections to ensure the CPW ground around these area are having the same potential. The bridges are 30 μm long and 5 μm wide. Two 8×9 μm openings are etched away from the SiO dielectric layers near the ends of the bridges to ensure the top TiN film is in electrical contact with the bottom film. (b) The re-simulate transmission profile of the TWPA with added bridges. (c) The predicted TWPA gain with $I_p = 0.45\, I_0$, showing higher peak gain, broader bandwidth and cleaner gain profile without gain ripples..

The gain profile shown in Fig. 5 (c) is also correspondingly cleaner with higher peak gain and broader operational bandwidth compared to the same plot for $I_p = 0.45\, I_0$ depicted in Fig. 4 (b). We can now achieve higher than 20 dB gain from approximately 0–8 GHz compared to 2.5–6.5 GHz shown previously without the bridges. This is almost twice broader the operational bandwidth, and the peak gain improved from approximately 28 dB to 38 dB, a 10 dB improvement. We believe these improvements are due to the less lossy transmission profile (the pump amplitude is hence much higher due to higher S_{21}), as well as the smoother wave-vector relation of the entire TWPA chip. We therefore conclude that in our case where the CPW gap is much narrower than the central strip width, it is essential to utilise equipotential bridges to make sure that the unwanted modes are suppressed and that the propagating waves are travelling along the long transmission line in pure CPW modes.

6. CONCLUSION

We have presented the design of our TiN KITWPA with the predicted gain-bandwidth product, transmission profile and the compression point along with the expected operational parameters. We first measured the transmission behaviour of the TWPA and found that the measured result does not agree with the simulation. The stopbands appeared at lower than expected frequencies, and the loss is higher. We believe that these unexpected behaviours are potentially caused by the difference between the expected thin film properties and the fabricated ones. Furthermore, we suspect that the chip could be inductively short due to the very narrow CPW gap width, and the lack of protection layer on top of the TiN film. Using the measured data and updated estimation of the resistivity and thickness, we re-simulate the performance of the TWPA, and successfully reproduce the transmission profile. We also found that equipotential bridges are crucial to ensure that the waves are propagating along the transmission in proper CPW modes, to prevent unexpected losses and variations in transmission amplitude. With these equipotential bridges, we believe that the TWPA can achieve higher than 20 dB gain with about 8 GHz bandwidth, albeit at lower central frequency of 4 GHz instead of the intended 8 GHz. Further experimental investigations are still currently underway at the time of writing, and a new batch of KITWPA will be fabricated with bridges and tested in coming months.

ACKNOWLEDGMENTS

The authors would like to thank the European Research Council (ERC) programme under the project number 803862 (SPA4AstroQIT) and the Foundation MERAC for supporting this research work. J. Longden's Ph.D. studentship is supported by the UK Science and Technology Facilities Council.

REFERENCES

[1] Noroozian, O., "Cycle 5 NRAO ALMA Development Study Report Technology Development of Quantum-Limited, Ultra-Wideband RF Amplifiers for ALMA: A 65-150 GHz Test Case,"

[2] Zobrist, N., Eom, B. H., Day, P., Mazin, B. A., Meeker, S. R., Bumble, B., LeDuc, H. G., Coiffard, G., Szypryt, P., Fruitwala, N., et al., "Wide-band parametric amplifier readout and resolution of optical microwave kinetic inductance detectors," *Applied Physics Letters* **115**(4), 042601 (2019).

[3] Noroozian, O., Kerr, A. R., Mangum, J. G., Day, P. K., Leduc, H. G., Zmuidzinas, J., Woody, D. P., Lichtenberger, A. W., Cyberey, M., and Weikle, R., "Superconducting parametric amplifiers: The next big thing in (sub)-millimeter-wave receivers," in [*2018 United States National Committee of URSI National Radio Science Meeting (USNC-URSI NRSM)*], 1–2, IEEE (2018).

[4] Che, G., Gordon, S., Day, P., Groppi, C., Jackson, R., Mani, H., Mauskopf, P., Surdi, H., Trichopoulos, G., and Underhill, M., "A superconducting phase shifter and traveling wave kinetic inductance parametric amplifier for w-band astronomy," *arXiv preprint arXiv:1710.11335* (2017).

[5] Bockstiegel, C., Gao, J., Vissers, M., Sandberg, M., Chaudhuri, S., Sanders, A., Vale, L., Irwin, K., and Pappas, D., "Development of a broadband nbtin traveling wave parametric amplifier for mkid readout," *Journal of Low Temperature Physics* **176**(3), 476–482 (2014).

[6] Backes, K., Palken, D., Al Kenany, S., Brubaker, B., Cahn, S., Droster, A., Hilton, G. C., Ghosh, S., Jackson, H., Lamoreaux, S., et al., "A quantum enhanced search for dark matter axions," *Nature* **590**(7845), 238–242 (2021).

[7] Kutlu, Ç., van Loo, A. F., Uchaikin, S. V., Matlashov, A. N., Lee, D., Oh, S., Kim, J., Chung, W., Nakamura, Y., and Semertzidis, Y. K., "Characterization of a flux-driven josephson parametric amplifier with near quantum-limited added noise for axion search experiments," *Superconductor Science and Technology* (2021).

[8] Braine, T., Cervantes, R., Crisosto, N., Du, N., Kimes, S., Rosenberg, L., Rybka, G., Yang, J., Bowring, D., Chou, A., et al., "Extended search for the invisible axion with the axion dark matter experiment," *Physical review letters* **124**(10), 101303 (2020).

[9] Fasolo, L., Greco, A., Enrico, E., Illuminati, F., Franco, R. L., Vitali, D., and Livreri, P., "Josephson travelling wave parametric amplifiers as non-classical light source for microwave quantum illumination," *arXiv preprint arXiv:2106.00522* (2021).

[10] Ranzani, L., Bal, M., Fong, K. C., Ribeill, G., Wu, X., Long, J., Ku, H.-S., Erickson, R. P., Pappas, D., and Ohki, T. A., "Kinetic inductance traveling-wave amplifiers for multiplexed qubit readout," *Applied Physics Letters* **113**(24), 242602 (2018).

[11] Devoret, M. H. and Schoelkopf, R. J., "Superconducting Circuits for Quantum Information: An Outlook," *Science* **339**(6124), 1169–1174 (2013).

[12] Esposito, M., Rahamim, J., Patterson, A., Mergenthaler, M., Wills, J., Campanaro, G., Tsunoda, T., Spring, P., Sosnina, S., Jebari, S., Ratter, K., Tancredi, G., Vlastakis, B., and Leek, P., "Development and characterization of a flux-pumped lumped element Josephson parametric amplifier," *EPJ Web Conf.* **198**, 00008 (2019).

[13] O'Brien, K., Macklin, C., Hover, D., Schwartz, M., Bolkhovsky, V., Zhang, X., Oliver, W., and Siddiqi, I., "Towards quantum-noise limited multiplexed microwave readout of qubits," in [*2016 IEEE MTT-S International Microwave Symposium (IMS)*], 1–3, IEEE (2016).

[14] Macklin, C., O'Brien, K., Hover, D., Schwartz, M. E., Bolkhovsky, V., Zhang, X., Oliver, W. D., and Siddiqi, I., "A near–quantum-limited Josephson traveling-wave parametric amplifier," *Science* **350**(6258), 307–310 (2015).

[15] Planat, L., Ranadive, A., Dassonneville, R., Puertas Martínez, J., Léger, S., Naud, C., Buisson, O., Hasch-Guichard, W., Basko, D. M., and Roch, N., "Photonic-Crystal Josephson Traveling-Wave Parametric Amplifier," *Phys. Rev. X* **10**, 021021 (Apr 2020).

[16] Eom, B. H., Day, P. K., LeDuc, H. G., and Zmuidzinas, J., "A wideband, low-noise superconducting amplifier with high dynamic range," *Nature Physics* **8**(8), 623–627 (2012).

[17] Zhao, S., Withington, S., Goldie, D. J., and Thomas, C. N., "Loss and saturation in superconducting travelling-wave parametric amplifiers," *Journal of Physics D: Applied Physics* **52**, 415301 (jul 2019).

[18] Shu, S., Klimovich, N., Eom, B., Beyer, A., Thakur, R., Leduc, H., and Day, P., "Nonlinearity and wideband parametric amplification in an NbTiN microstrip transmission line," *Physical Review Research* **3** (02 2021).